Supporting Information

Electron affinity regulation on ultrathin manganese oxide nanosheets toward ultra-stable pseudocapacitance

Kang Xiao,[a,b] Shen-Long Zhao,[d] Meizhi Cao,[a] Liang Zhang,[a] Nan Li, [a,b] Zhao-Qing Liu*[a,b,c]

[a]School of Chemistry and Chemical Engineering, Guangzhou University, Guangzhou 510006, China.

E-mail: lzqgzu@gzhu.edu.cn

[b]Guangzhou Key Laboratory for Clean Energy and Materials, Guangzhou University, Guangzhou 510006, China.

[c]Key Laboratory for Water Quality and Conservation of the Pearl River Delta, Ministry of Education, Guangzhou University, Guangzhou 510006, China

[d]School of Chemistry, The University of Sydney, Sydney 2006, Australia.

Experimental Section

1. Materials synthesis

1.1 Chemicals: All chemicals are analytical grade and used as received without further purification.

1.2 Synthesis of MnO_2 and F substituted MnO_2.

The FTO conductive glass was cleaned with ethanol, acetone and deionized (DI) water, under ultrasonication. Electrodeposition was conducted using a CHI 760E model Electrochemical Workstation (Shanghai) with two-electrode system, a carbon rod as the counter electrode and a piece of clean FTO (0.2 cm×1.0 cm×2.0 cm) as the working electrode. The MnO_2 nanosheets were electrodeposited in a solution containing 0.01 M $Mn(CH_3COO)_2$ + 0.02 M CH_3COONH_4 + DMSO (wt.10%) with a constant current of 0.8 mA for 60 min at 70 °C. The synthesis of F substituted MnO_2 are similar to that of MnO_2 by using 0.01 M $Mn(CH_3COO)_2$ + 0.02 M NH_4F + DMSO (wt.10%) as electrolyte. To distinguish, F substituted MnO_2 is denoted as MnOF.

2. Characterization

The surface morphology and structure of the samples were analyzed by the field emission scanning electron microscopy (FE-SEM, Quanta 400) and transmission electron microscopy (TEM, FEI, Tecnai™ G2F30). The crystallographic structure of the samples was analyzed using powder X-ray diffraction (XRD, Bruker, D8 ADVANCE) with Ka radiation (λ = 1.5418 Å). The chemical state and composition of the products were analyzed by X-ray photoelectron spectroscopy (XPS, ESCALab250). EPR tests were carried out in the X-band (9.45 GHz) with 5.00-G modulation amplitude and a magnetic field modulation of 100 kHz using a Bruker, A300-10-12 Bruker EPR spectrometer at 77 K. The microwave power was 5.00 mW.

The XAFS spectra of sample at the Mn K-edge (photoelectron energy origin E0 = 6,539 eV) were performed at the BL14W1 beamline of Shanghai Synchrotron Radiation Facility operated at 3.5 GeV with a constant current of 240 mA. EXAFS data were fit with Artemis software. Ab initio phases and amplitudes were used in the EXAFS equation to fit experimental data:

$$\chi(k) = \sum_{\Gamma}[\frac{N_{\Gamma}S_0^2F_{\Gamma}(k)}{2kR_{\Gamma}^2}e^{-2k^2\sigma_{\Gamma}^2}e^{-2R_{\Gamma}/\lambda(k)} \times \sin(2kR_{\Gamma} + \phi_{\Gamma}(k))]$$

Γ is the summation over the individual scattering pathways, k is the photoelectron wavevector. $F(k)$, $\lambda(k)$ and $\Phi(k)$ are the scattering amplitude, mean free path of inelastically-scattered photoelectrons and is the phase shift, respectively. S_0^2 is the amplitude reduction factor, degeneracy (N), half-path length (R), energy shift parameter (E_0), and mean-squared disorder (σ^2, set as Debye-Waller factor), were fitted in order to extract the local structural information.

3. Electrochemical measurements

The electrochemical tests were performed in a three-electrode electrochemical cell using a Pt mesh, a SCE electrode and as-prepared samples as a counter electrode, a reference electrode and working electrode, respectively in 0.5 M Na_2SO_4 aqueous solution. Cyclic voltammetry (CV) and galvanostatic charge-discharge (GCD) were measured to determine the charge storage capabilities and stabilities of the as-prepared materials. Electrochemical impedance spectroscopy (EIS) measurements were carried out in the frequency range of 0.01Hz-100 kHz with perturbation AC voltage of 10 mV.

4. Calculations

The specific capacitance can be calculated according to the following equation:

$$C_s = I\Delta t/S\Delta V$$

Where Cs (F cm^{-2}) is the areal capacitance, S (cm^2) is the area of active materials, ΔV (V) is the potential window, I (A) and Δt (s) are constant discharging current and discharging time, respectively.

5. DFT calculations

The DFT calculations were performed by using Cambridge Sequential Total Energy Package (CASTEP) code. The geometrical structures of MnO_2 slab structure was optimized with the Perdew-Burke-Ernzerhof (PBE) of the generalized gradient approximation (GGA). The plane wave cutoff energy was fixed as 500 eV, and the Monkhorst-Pack k-point was set to be 4 × 4 × 1. Convergence criteria of the Hellmann–Feynman force of the system was 10 meV/Å. Supercells are composed of 6-atomic-layer-thick slabs separated by ~20 Å of vacuum perpendicular to the surface to avoid the effect of unphysical charge dipoles. Bottom layers of the MnO_2 slab were fixed, but the top two MnO_2 monolayers atoms and adsorbed Na atoms were allowed to move freely. For the electronic structure calculation, the hybrid functional (HSE06) was adopted to overcome band gap underestimation brought by conventional LDA or GGA pseudopotential. In this study, the intercalation energy is calculated by:

$$E_{int} = \frac{E_{MnO2/Na} - (E_{MnO2} + nE_{Na})}{nNa}$$

Where, E_{int} is the calculated intercalation energy, $E_{MnO2/Na}$ is the energy of the MnO_2 supercell with n intercalated Na ions, E_{MnO2} is the energy of the bare MnO_2 supercell, n is the number of Na ions and E_{Na} is the energy of one Na ion in metallic bcc Na. The intercalation energy of F-doped MnO_2 slab structure could be calculated likewise.

MnO$_2$

M ion solution (K$^+$, Na$^+$, H$^+$)

substrate

MnOOM

Mn^{2+}

substrate

Charge-discharge process:

$$Mn(IV)O_2 + M^+ + e^- \underset{2}{\overset{1}{\rightleftharpoons}} Mn(III)OOM$$

Dissolution process:

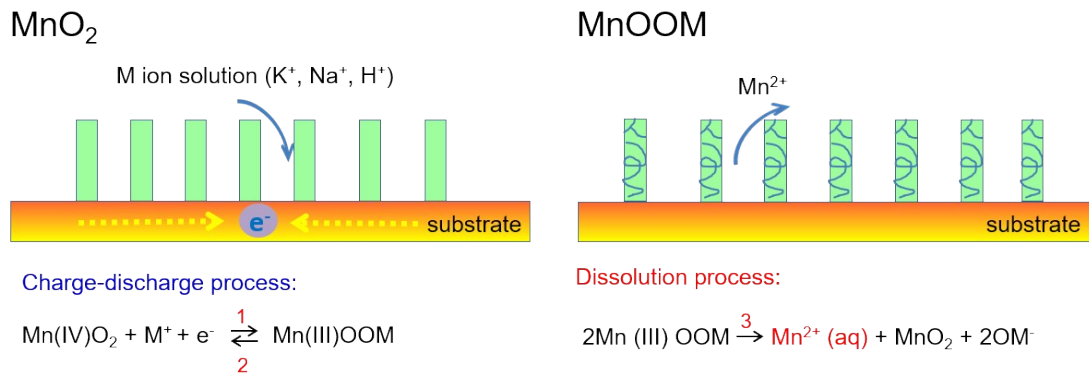$$2Mn(III)OOM \xrightarrow{3} Mn^{2+} (aq) + MnO_2 + 2OM^-$$

Figure S1. Schematic illustration of the charging and discharging process and dissolution process of MnO$_2$ electrode.
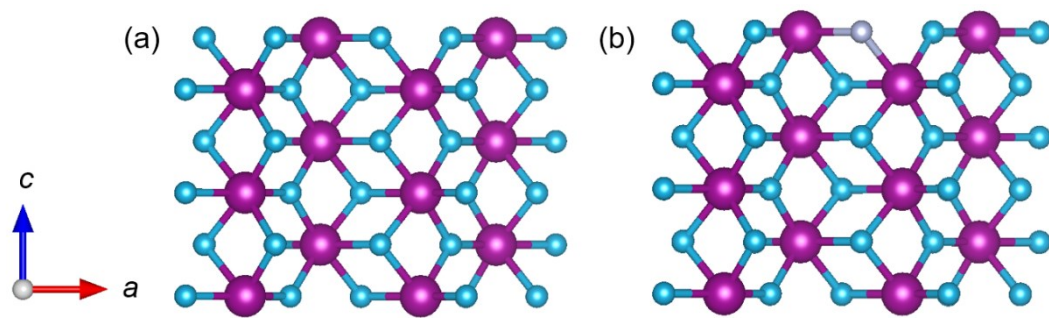
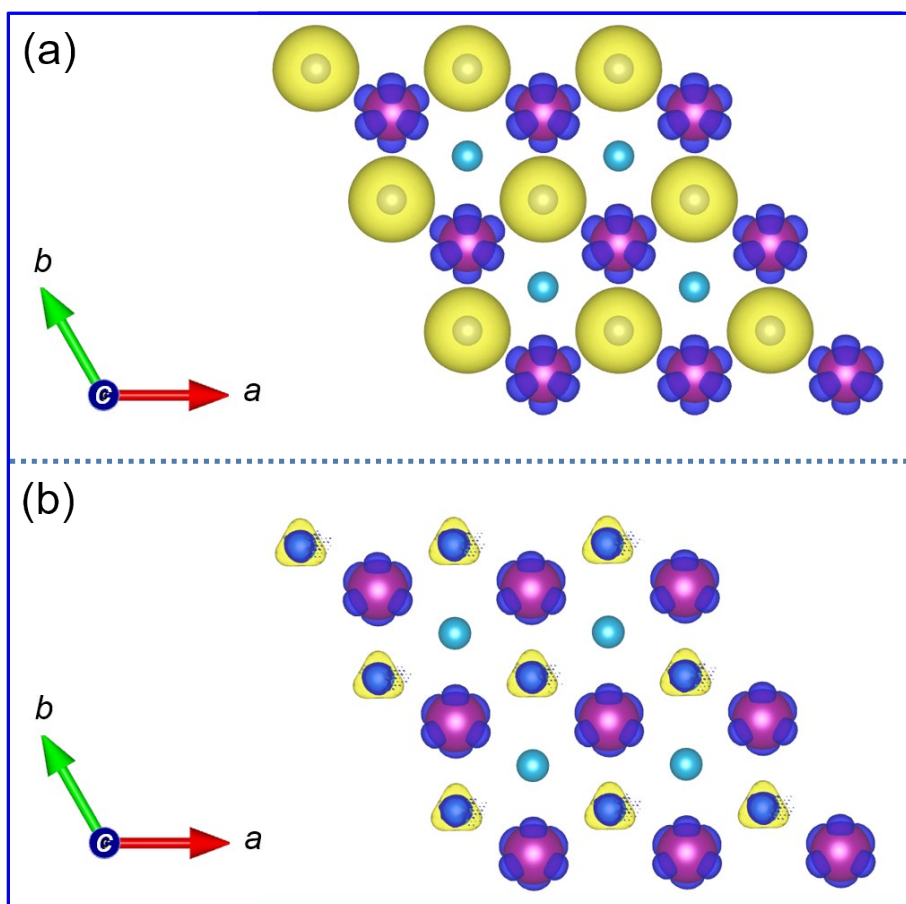Figure S2. Schematic illustration of the structures of pure MnO_2 (a) and F-substitutive MnO_2.

Figure S3. Differential charge densities of the F substituted MnO_2 and b) the MnO_2. Bule color indicates the loss of electrons whereas yellow shows the gain of electrons.
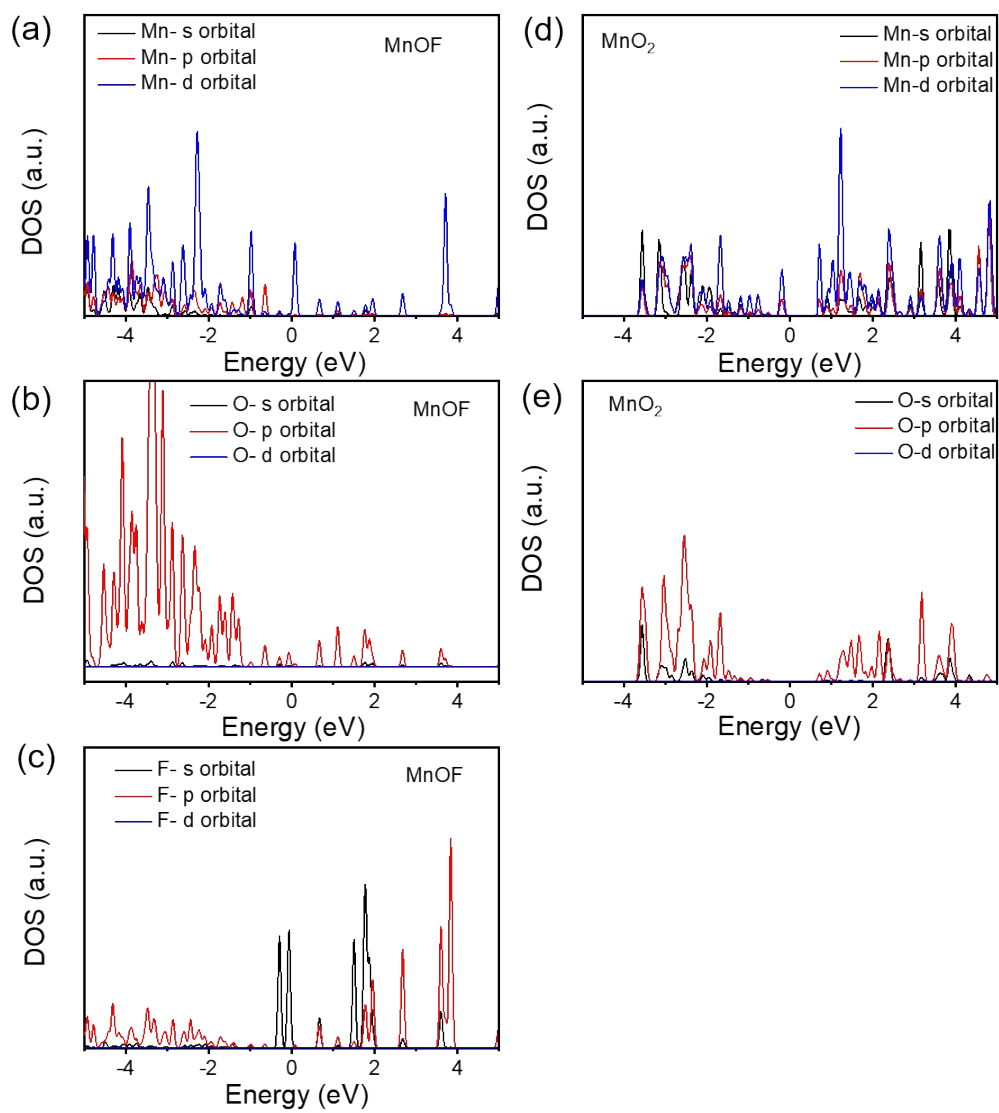
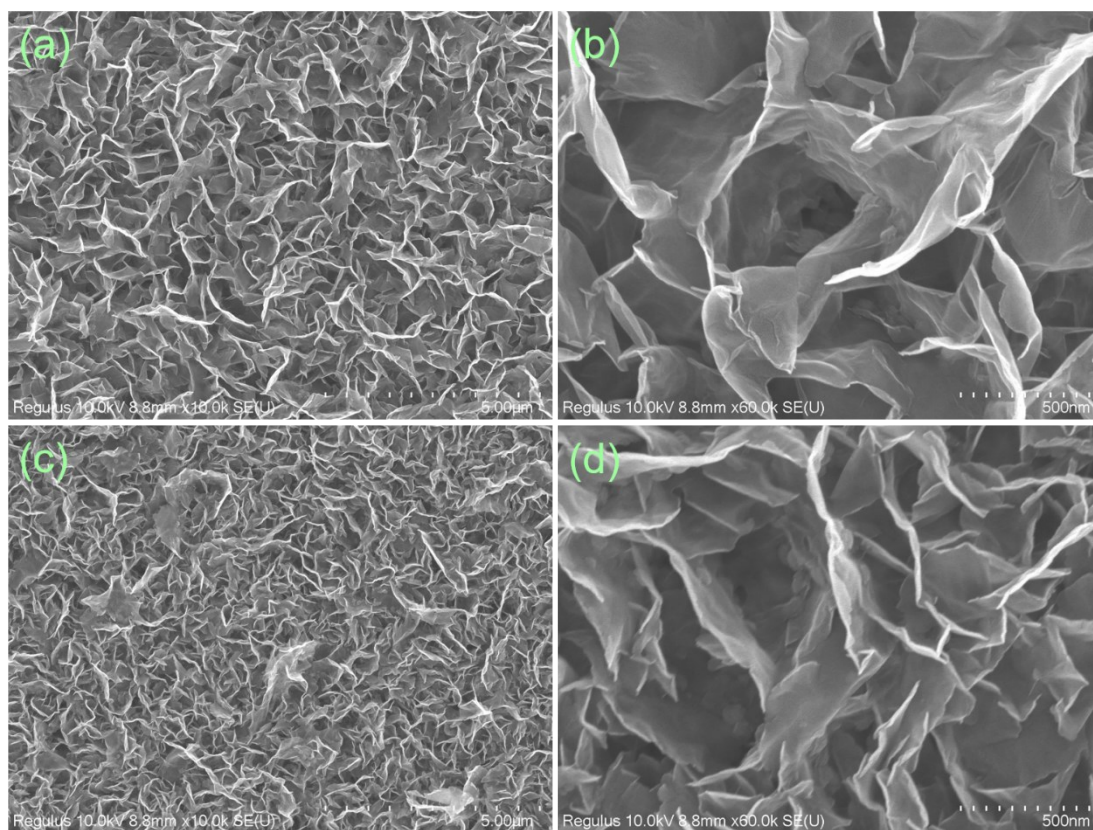Figure S4. Partial DOS of (a-c) MnOF nanosheets and (d-e) MnO$_2$ nanosheets.

Figure S5. SEM images of MnO$_2$ nanosheets (a-b) and MnOF nanosheets (c-d).
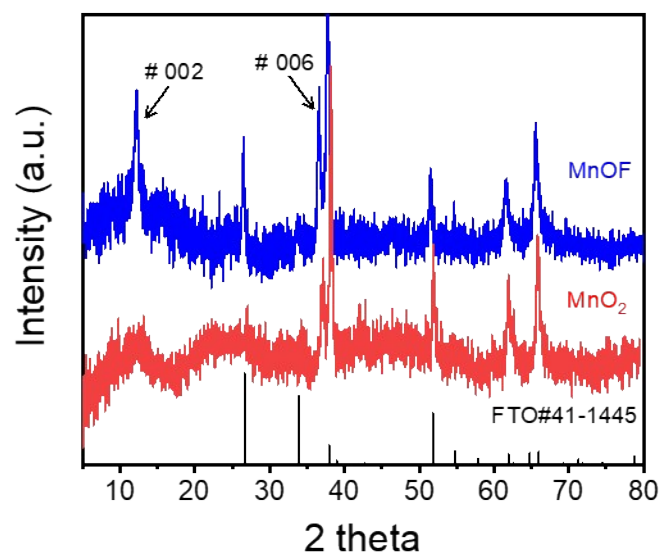
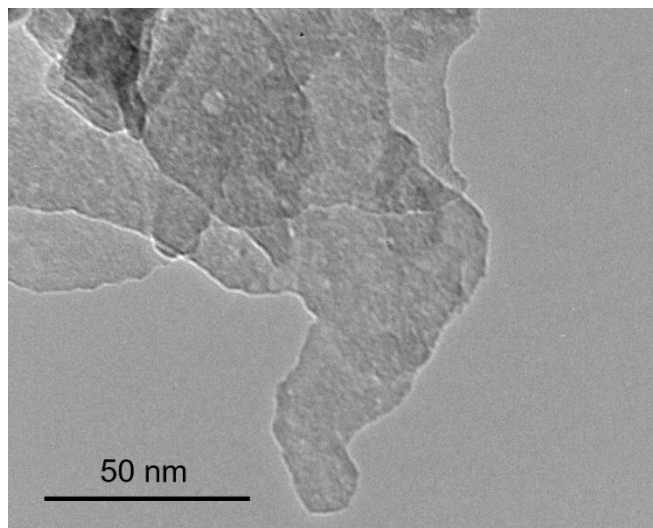Figure S6. XRD patterns of the MnO$_2$ and MnOF nanosheets on FTO conductive glass.
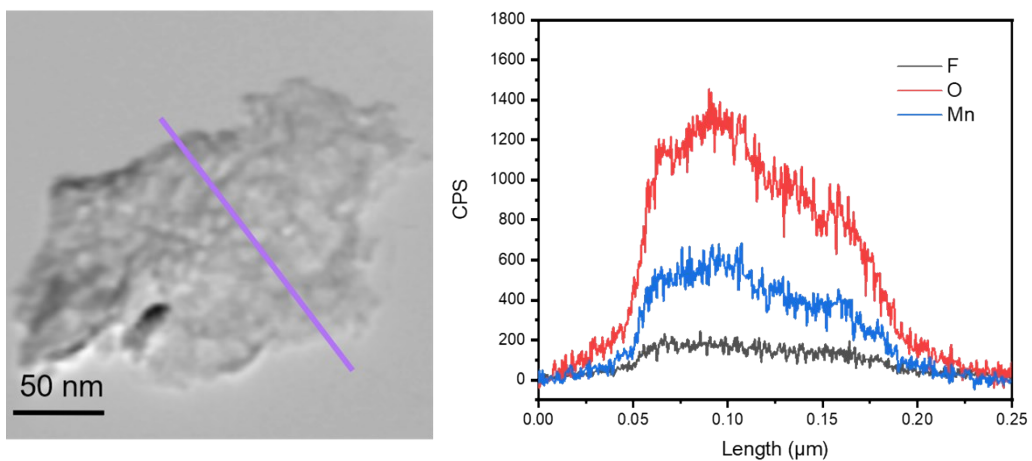
Figure S7. TEM images of MnO$_2$.

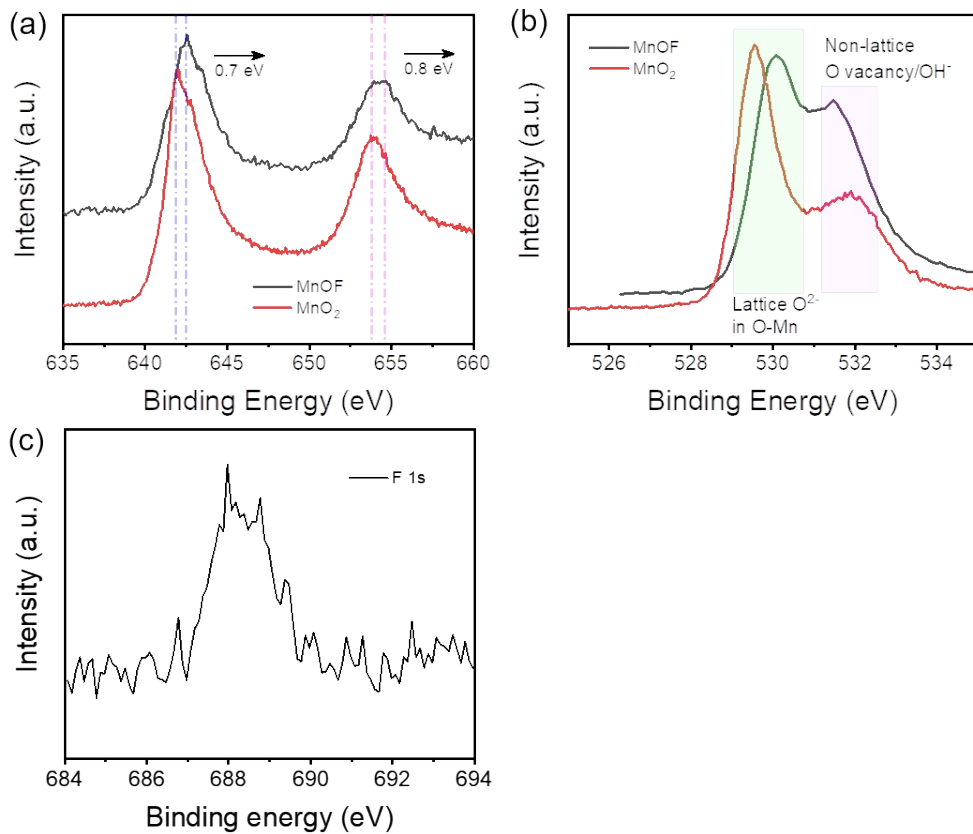Figure S8. EDS line-scanning profile of a single MnOF nanosheet.

Figure S9. (a) XPS spectra of Mn 2p, and (b) O 1s for the as-prepared MnO_2 and (F) MnOF nanosheets.

The spin orbit of Mn 2p splits into Mn $2p_{1/2}$ and Mn $2p_{3/2}$ at 654 and 642.2 eV with a spin energy separation of ~11.8 eV, which indexs to Mn^{4+} and is consistent with literature.[1] The F 1s peak located at 688.5 eV was attributed to the substitute F atoms that occupied oxygen sites in the MnO_2 crystal lattice rather than adsorbed on the surface.[2]

Table S1. Fitting Results of Mn K-Edge EXAFS Data.[a]

Sample	Shell	N	R[Å]	$\sigma^2[\text{Å}^2]$	$\triangle E_0[eV]$
MnOF	Mn-O	5.92	1.86	3.62	-8.63
	Mn-Mn	4.99	2.72	5.15	-4.23
MnO$_2$	Mn-O	5.95	1.88	3.12	-9.26
	Mn-Mn	5.52	2.79	5.06	-5.12

[a]The lengths of Mn-O bonds and coordination numbers of Mn atoms were extracted from EXAFS curve-fitting for MnO$_2$ and MnOF. R, the length of Mn-O bonds and Mn-Mn bonds; N, the coordination number of Mn atoms corresponding to the Mn-O bonds; σ^2, the Debye-Waller factor; ΔE0, the inner potential correction.
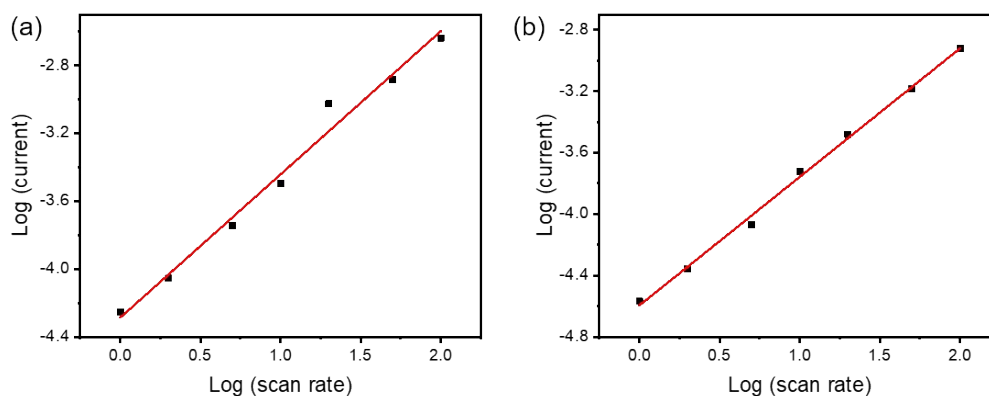
Figure S10. Determination of the b-value using the relationship between peak current and scan rate for (a) MnOF, and (b) MnO$_2$.

The total charge stored can be separated into two main components: (i) pseudocapacitive component due to fast Faradaic charge-transfer process with surface atoms, and non-Faradaic contribution from the double layer adsorption of ions. (ii) Diffusion-controlled Faradaic intercalation processes. The measured current i from CV curves obeys power law relationship with the sweep rate, v. [3]

i = ab^v

where "a" and "b" are adjustable parameters. For diffusion-controlled processes, the current response is proportional to the square root of the scan rate (b = 0.5); on the other hand, for a capacitive process, the current response is proportional to the scan rate (b = 1). As shown in Figure S11, the b value for both MnOF and MnO$_2$ at scan rates from 1 to 100 mV s^{-1} is 0.86 and 0.84, suggesting that the current response is mainly capacitive.
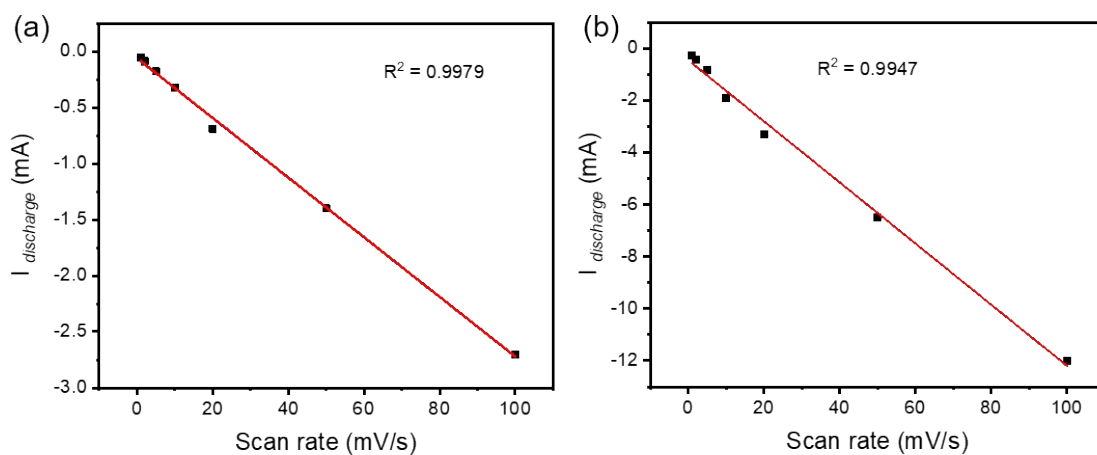
Figure S11. The relationship between discharge current and scan rate for (a) MnOF, and (b) MnO$_2$.

Note: the discharge current extracted from the CV profile at potential of the current density of the electrode at 0.4V.
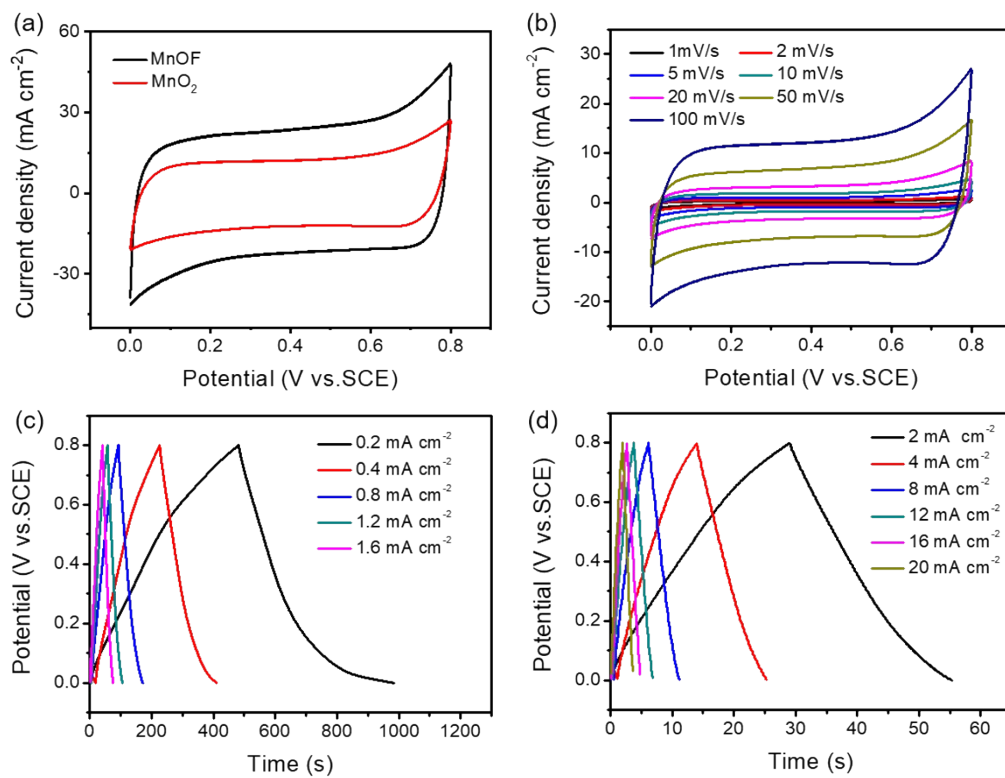
Figure S12. (a) CV curves of MnO_2 and MnOF electrode at scan rate of 50 mV/s. (b) CV curves of MnO_2 electrode under different scan rates. (c-d) GCD curves of MnO_2 electrode under different current density.
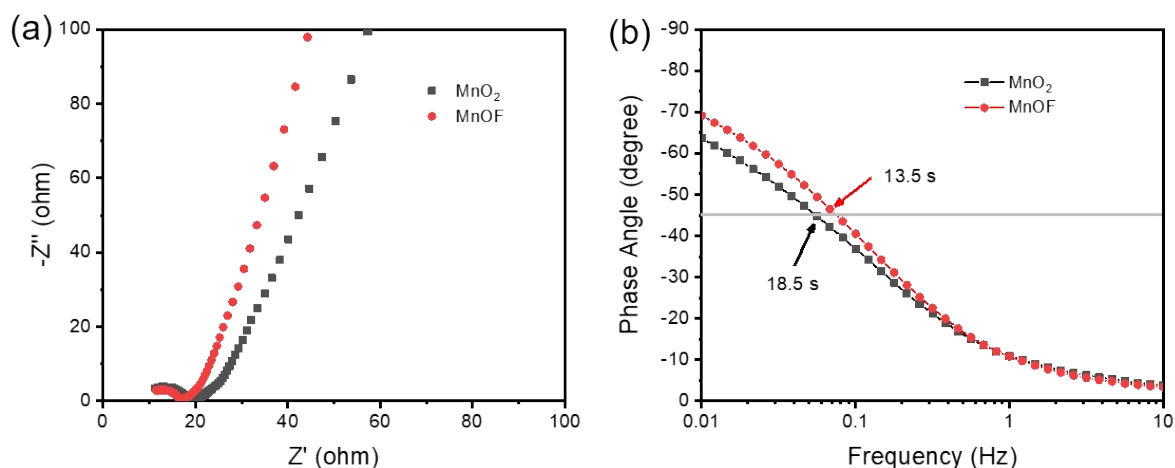
Figure S13. (a) Nyquist plot of MnOF and MnO$_2$ electrode. (b) Bode plots of phase angle versus frequency for MnOF and MnO$_2$ electrode.

The MnOF electrode shows lower resistance (Rct = 13.7 Ω) than MnO$_2$ (Rct = 19.6 Ω). The slope of the MnOF electrode in comparison with MnO$_2$ electrode nearly vertical in the low-frequency region, indicating that the MnOF possess better ion diffusion behavior.[4] The characteristic frequency, f_0, for a phase angle of -45° is 0.074 Hz for the MnOF. The corresponding time constant τ_0 (=1/f_0) was calculated as 13.5 s, compared with 18.5 s (0.054 Hz at -45°) for the pure MnO$_2$. Thus, F replacing O atoms in MnO$_2$ enhances the electrolyte ion transport rate in the supercapacitor.
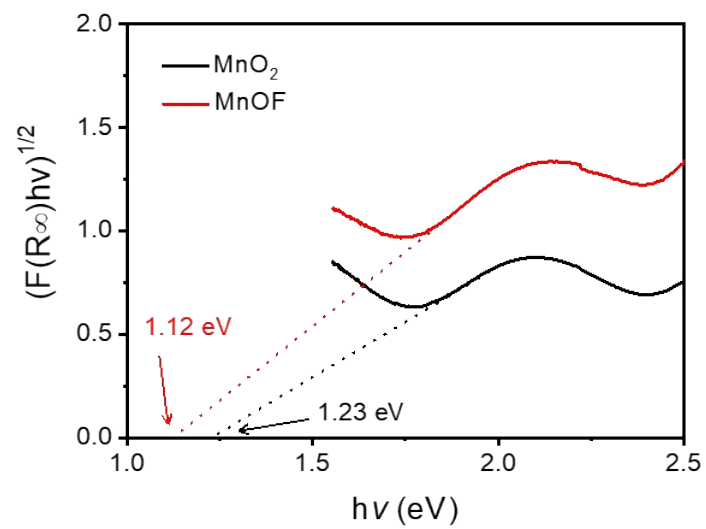
18

Figure S14. plots (ah$v$)^2 vs photo energy (hv) of the MnO$_2$ and MnOF nanosheets. The band gaps of MnOF were narrowed from 2.61 (MnO$_2$) to 2.09 eV.
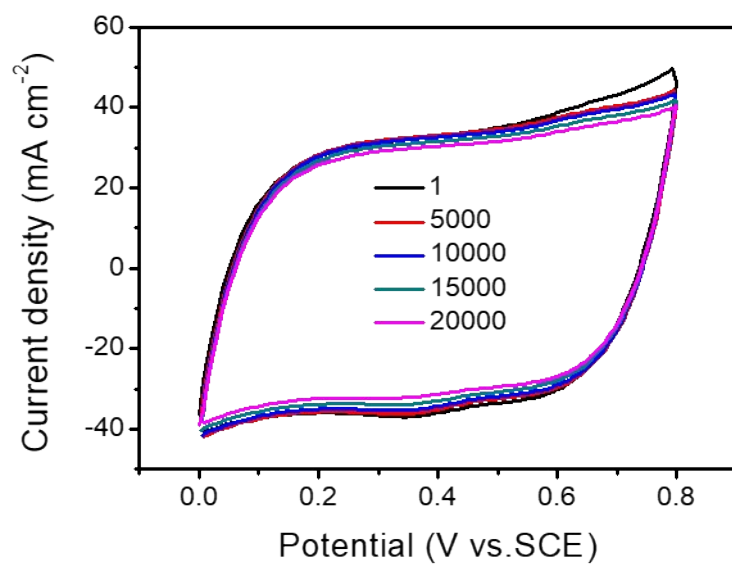
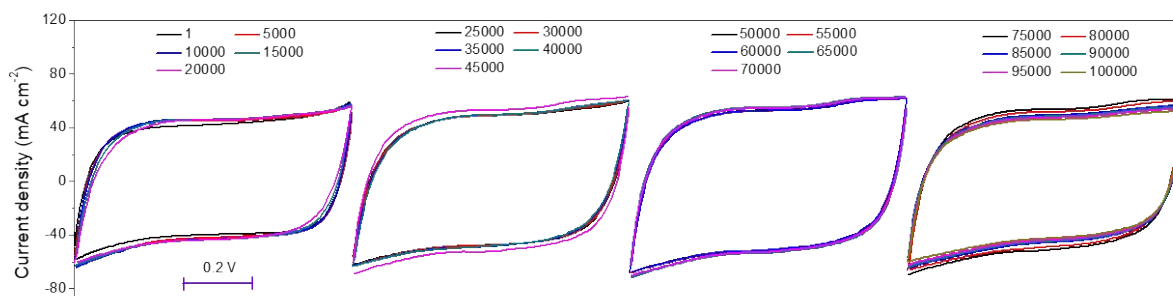Figure S15. Representative CV curves of MnO$_2$ nanosheets.

Figure S16. Representative CV curves of MnOF.

It was found that there was almost no decrease of the area of CV curves with the increment of the cycle number (In the first 20,000 cycles, the area of the curve increases gradually due to the activation process of the electrode) and 15 % of the initial specific capacitance remained after 100 000 cycles in the range of 0-0.8 V in 0.5 M Na_2SO_4 aqueous solution by repeated cycling processes at a high scan rate of 200 mV/s. This further demonstrated that the MnOF was a super stable electrode material.
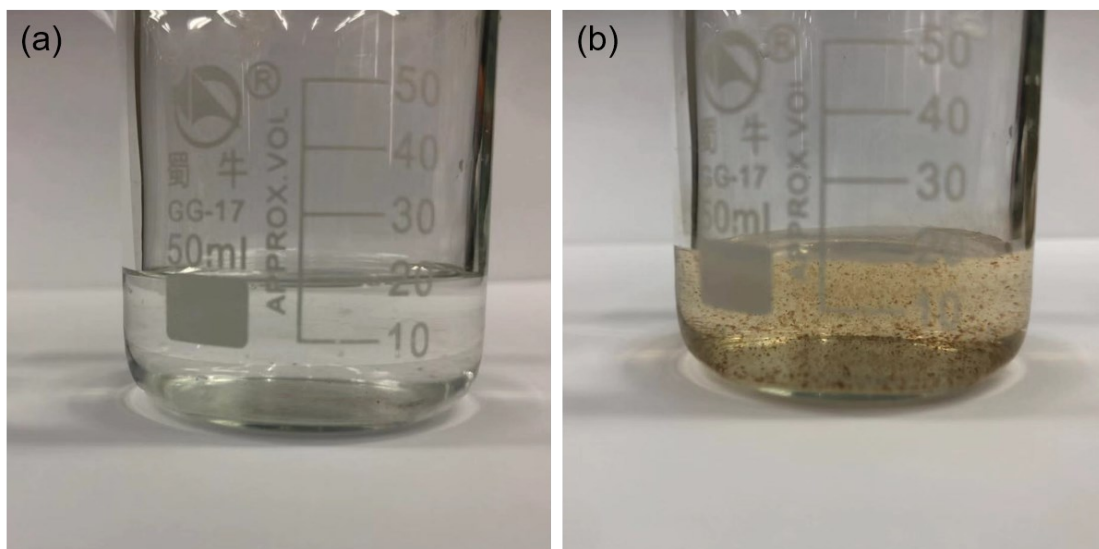
Figure S17. The optical photograph of electrolyte after cycling tests, (a) MnOF, (b) MnO$_2$.
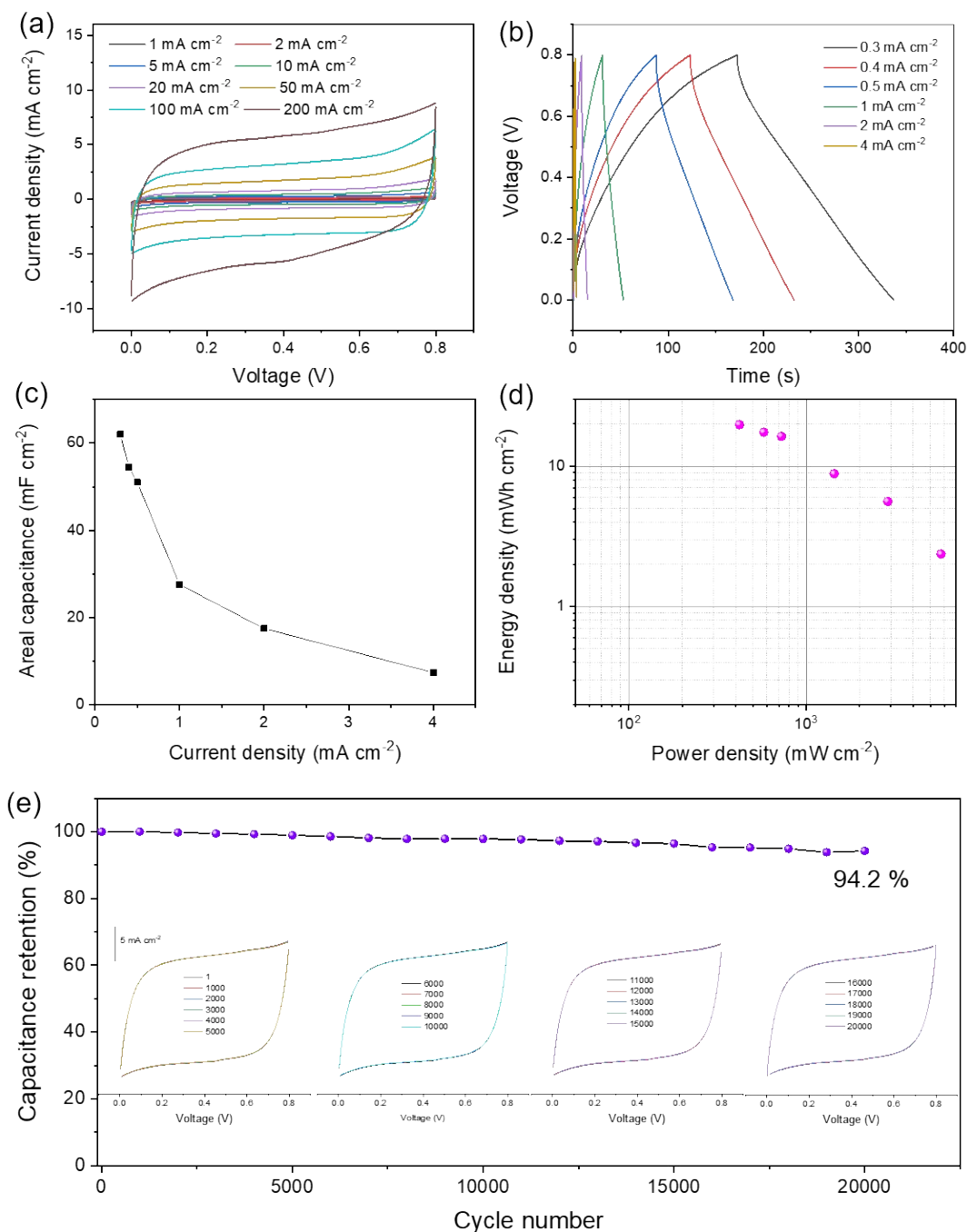
Figure S18. (a) Cyclic voltammetry plots at different scan rates, (b) Charging-discharging curves at different current densities, (c) specific capacitance (d) Ragone plot and (e) cycling stability of the MnOF based SSC devices.

The CV and GCD profiles indicate that the SSC device exhibits pseudocapacitive behavior. The specific capacitance of the MnOF SSC, calculated from the GCD profiles, are shown in **Figure S18a-b**. The maximum specific capacitance for the SSC device is 61.95 mF cm^{-2} at 0.3 mA cm^{-2}. **Figure S18d** shows the energy density and power density of the assembled MnOF

SSCs, presented as Ragone plots. The maximum energy density of the SSC device is 19.82 mWh cm^{-2}. The ability of the assembled devices to endure a long-term cycling test is the main indicator of supercapacitor device performance. The stability curves strongly indicate that approximately 94.2 % of the initial capacitance of the device, is retained after 20000 cycles at a scan rate of 200 mV s^{-1}, confirming its superior cycling performance.

Table S2. ICP-MS results of the electrolyte after the long-term durability.

Sample	The concentration of Mn
MnOF	119.7 ppm
MnO$_2$	264.3 ppm

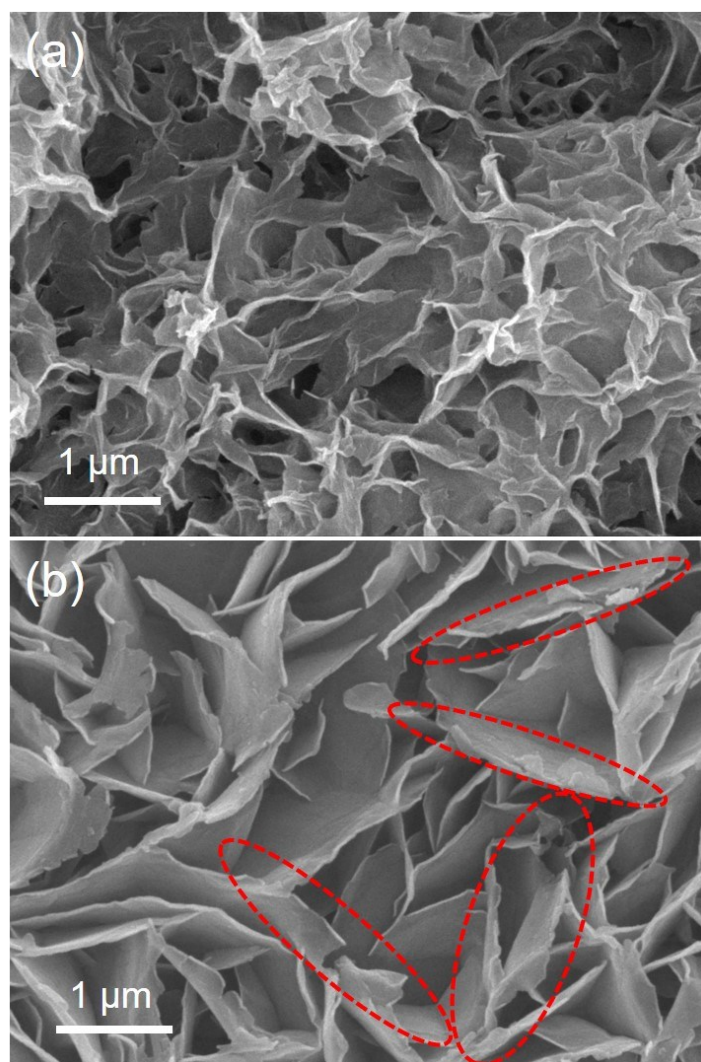Note: The measured solution was diluted by 1% HNO$_3$ and then measured by ICP-MS

(ThermaFisher iCAP Q)

Figure S19. SEM images of the post-cycling (a) MnO$_2$ nanosheets and (b) MnOF nanosheets.

It can be seen that the construction of MnO$_2$ nanosheets was obviously dissolved after 20,000 cycles. For MnOF nanosheets, there is only the edge of nanosheets is rough slightly compared to original MnOF, as the examples shown in the red circles.
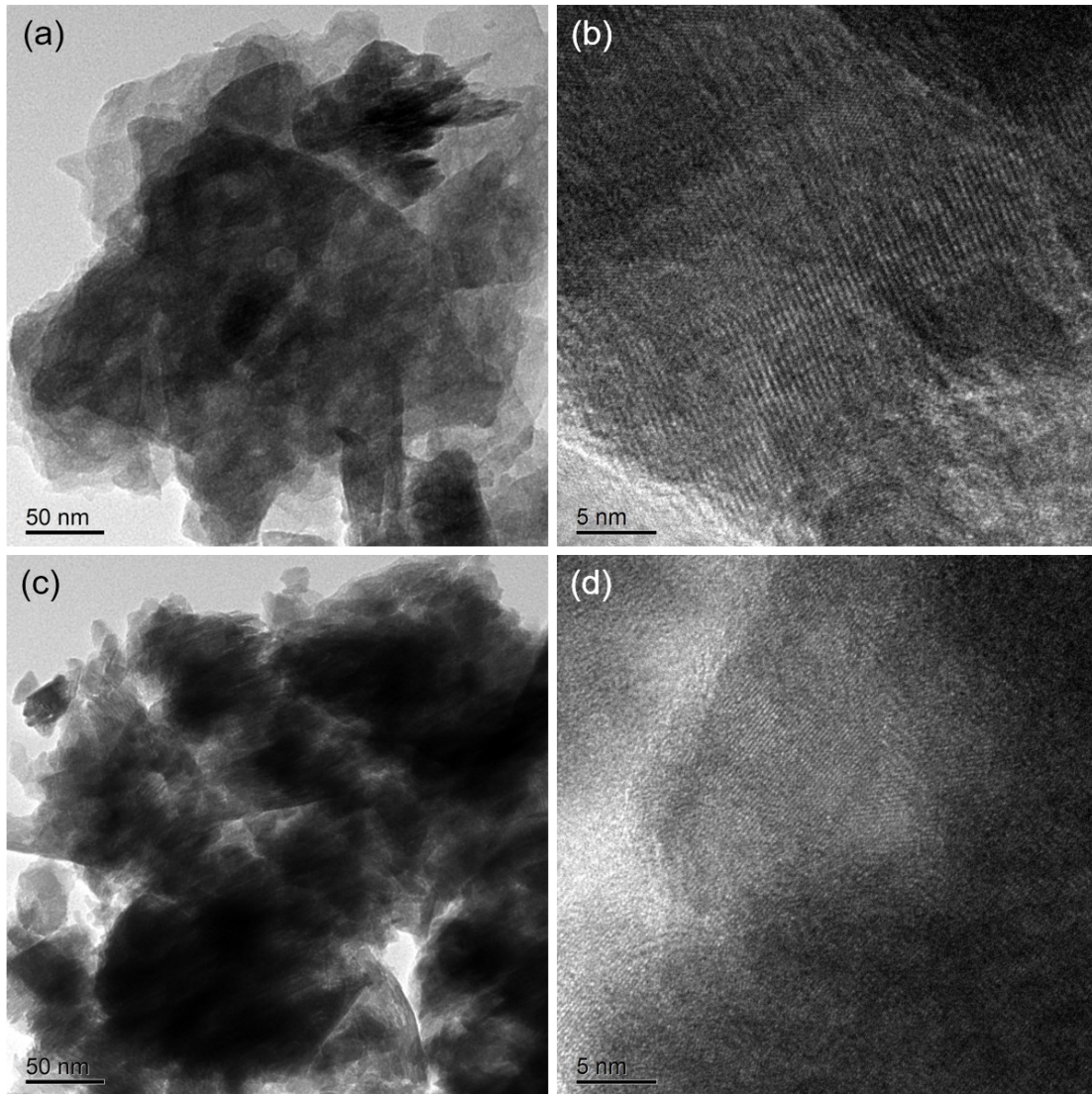
Figure S20. TEM and HR-TEM images of the post-cycling (a-b) MnOF nanosheets and (c-d) MnO$_2$ nanosheets.

The HR-TEM results show that the MnOF electrode can still observed clear lattice fringes after a long period of cycling, while the MnO$_2$ electrode shows more disordered structure.
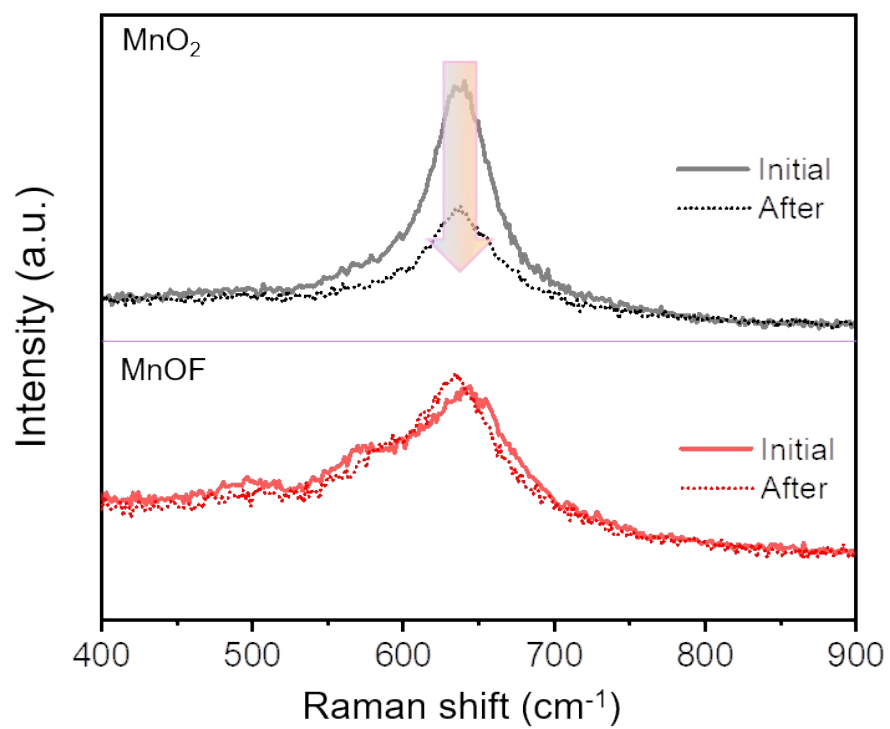
Figure S21. Raman results of the post-cycling MnOF nanosheets and MnO_2 nanosheets.
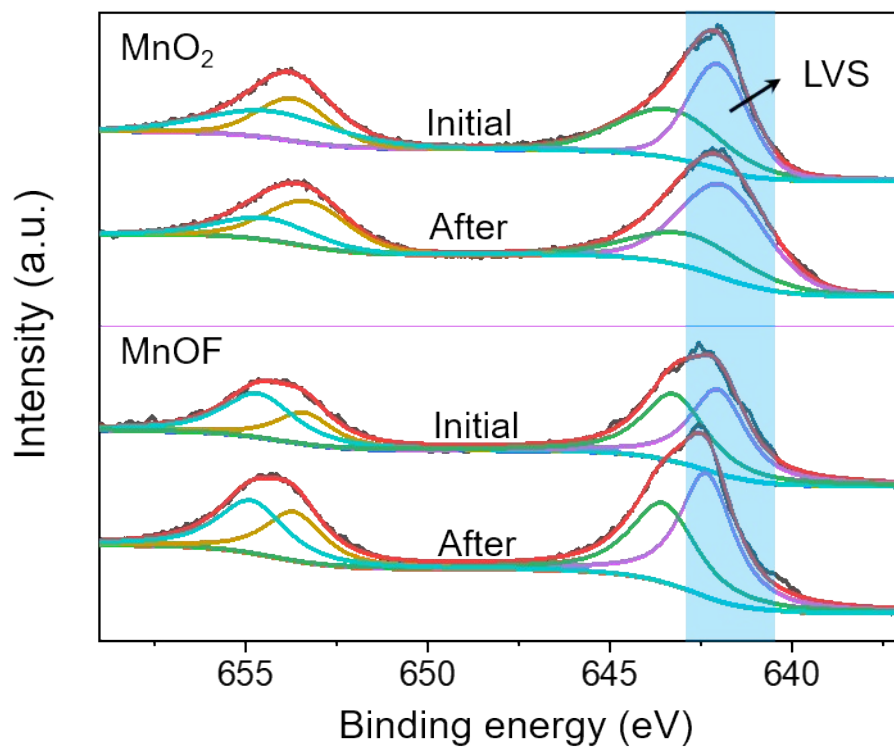
Figure S22. XPS results of the post-cycling MnOF nanosheets and MnO$_2$ nanosheets.

Table S3. XPS fitting spectral parameters of Mn and O species.

| Sample		Mn 2p$_{3/2}$		Mn 2p$_{1/2}$	
		Mn^{3+}	Mn^{4+}	Mn^{4+}	Mn^{4+}
MnO$_2$	Binding energy	642	643.5	653.7	654.7
	Relative % Composition	35.4	28.2	16.8	19.6
MnO$_2$ after cycles	Binding energy	642	643.2	653.4	654.7
	Relative % Composition	45.4	21.6	20.9	12.1
MnOF	Binding energy	642.1	643.1	653.5	654.8
	Relative % Composition	33.6	30.6	13.2	22.6
MnO$_2$ after cycles	Binding energy	642.3	643.5	653.7	654.9
	Relative % Composition	36.3	28.3	15.8	19.6
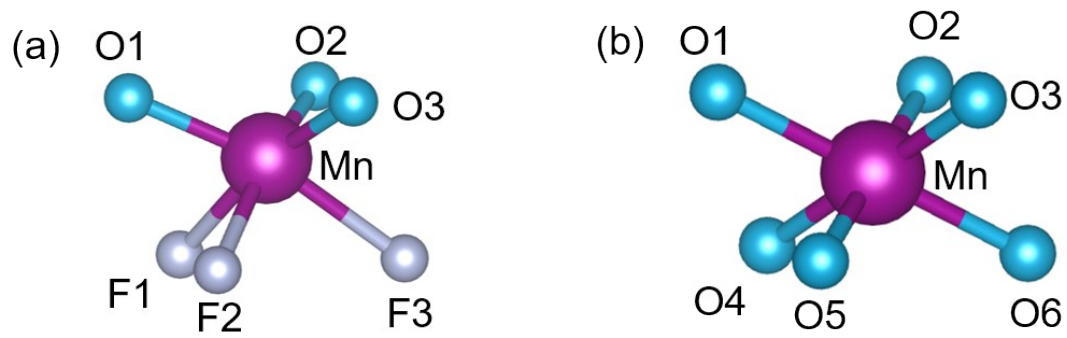
Figure S23. Schematic illustration of $[Mn(OF)_6]$ and $[MnO_6]$ octahedron.

Table S4. The bond length of [Mn(OF)$_6$] and [MnO$_6$] octahedron.

MnO$_2$		MnOF	
Mn-O1	1.84366	Mn-O1	1.81376
Mn-O2	1.84369	Mn-O2	1.81377
Mn-O3	1.84369	Mn-O3	1.81377
Mn-O4	1.84361	Mn-F3	2.05672
Mn-O5	1.84357	Mn-F2	2.05672
Mn-O6	1.84357	Mn-F1	2.05673

Table S5. The bond angle of [Mn(OF)$_6$] and [MnO$_6$] octahedron.

MnO$_2$		MnOF	
O1-Mn-O2	101.1834	O1-Mn-O2	104.1
O1-Mn-O3	101.1834	O1-Mn-O3	104.1
O1-Mn-O6	179.9933	O1-Mn-F3	167.8359
O1-Mn-O5	78.8142	O1-Mn-F2	83.1563
O1-Mn-O4	78.8142	O1-Mn-F1	83.1563
O2-Mn-O3	101.1825	O2-Mn-O3	104.0997
O2-Mn-O6	78.8125	O2-Mn-F3	83.1563
O2-Mn-O5	179.9942	O2-Mn-F2	167.8357
O2-Mn-O4	78.8129	O2-Mn-F1	83.1563
O3-Mn-O6	78.8125	O3-Mn-F3	83.1561
O3-Mn-O5	78.8129	O3-Mn-F2	83.1563
O3-Mn-O4	179.9942	O3-Mn-F1	167.8358
O6-Mn-O5	101.1899	F3-Mn-F2	88.1179
O6-Mn-O4	101.1899	F3-Mn-F1	88.118
O5-Mn-O4	101.1916	F2-Mn-F1	88.118

References

[1]   a) K. Xiao, L.-X. Ding, H. Chen, S. Wang, X. Lu, H. Wang, *J. Mater. Chem. A* **2**016, **4**, 372;

b) K. Xiao, J.-W. Li, G.-F. Chen, Z.-Q. Liu, N. Li, Y.-Z. Su, *Electrochim. Acta* 2014, **149**, 341.

[2]   D.-G. Huang, S.-J. Liao, J.-M. Liu, Z. Dang, L. Petrik, *J. Photochem. Photobio. A* 2006, **184**, 282.

[3]   Q. Zhang, Z. Liu, B. Zhao, Y. Cheng, L. Zhang, H.-H. Wu, M.-S. Wang, S. Dai, K. Zhang, D. Ding, Y. Wu, M. Liu, *Energy Storage Mater.* 2019, **16**, 632.

[4]   D. N. Futaba, K. Hata, T. Yamada, T. Hiraoka, Y. Hayamizu, Y. Kakudate, O. Tanaike, H. Hatori, M. Yumura, S. Iijima, *Nat. Mater.* 2006, **5**, 987.